ISSN 0965-545X, Polymer Science, Series A, 2024. © Pleiades Publishing, Ltd., 2024.

COMPOSITES

Development of a Nanocomposite Material Based on PCL/Zeolite-Supported Silver Nanoparticles for Active Food Packaging

Fayçal Benhacine[a],*, Feriel Meriem Lounis[a], and Assia Sihem Hadj-Hamou[a]

[a] Laboratory of Polymer Materials, Faculty of Chemistry,
University of Sciences and Technology Houari Boumediene, BP 32 El-Alia, Algiers, Algeria
**e-mail: faycal.benha@gmail.com*

Received March 3, 2024; revised April 11, 2024; accepted May 2, 2024

Abstract—In recent years, more and more researchers devote attention on the development and application ofbiodegradable, renewable, abundant, environmental-friendly and low-cost active packaging films, with appropriate antioxydante and antimicrobial properties. This paper focuses on developing composite poly (ε-caprolactone) (PCL) membranes reinforced with silver-zeolite nanoparticles (AgZ) prepared by solvent casting method. The resulting structural, thermal and surface properties of the nanocomposite materials were studied by using experimental characterization techniques such as Fourier-transform infrared (FTIR) analysis, UV-visible spectrophotometry, X-Ray diffraction (XRD), contact angle (CA), atomic force microscopy (AFM), thermogravimetric analysis (TGA), and differential scanning calorimetry (DSC). The water vapor permeability (WVP) and the mechanical properties have been investigated. Experimental results showed that AgZ nanoparticles were well dispersed into PCL matrix leading to thermally stable nanocomposites with semi-crystalline structure and hydrophilic surfaces. More importantly, the nanocomposite films showed good antibacterial activity against *Staphylococcus aureus* and *Salmonella enteric* strains, demonstrating a potential application as an effective and safe packaging material to prolong the shelf life of food products.

DOI: 10.1134/S0965545X24600649

INTRODUCTION

Every year, around one-third of the produced food is wasted, globally due to several factors such as environmental conditions, mechanical damage, transportation, microbial decay or oxidation [1]. Advanced food packaging technology, such as eco-friendly biodegradable nanocomposite materials [2], ensures food safety from pollutants and microbial pathogens, extending the shelf-life period of the preserved foods. Indeed, the incorporation of antimicrobial and antioxidant agents, such as metal oxide nanoparticles [3, 4] or essential oils [5], into polymer matrices used in food packaging represents an effective method to develop polymers with antimicrobial properties. Particularly, the use of zeolites for different food applications, such as fillers for food packaging materials, have attracted the attention of researchers [6].

Zeolites are microporous crystalline aluminosilicates made up of AlO_4 and SiO_4 tetrahedral units [7, 8]. These fundamental tetrahedral frameworks are linked by oxygen atoms, which form regular intracrystalline cavities and channels of molecular dimensions [9]. The non-equivalent isomorphous substitution of Al^{3+} for Si^{4+} in the tetrahedra generates a negative charge of the framework. This negative charge is balanced by the presence of cations, mainly Na^+, K^+, Ca^{2+}, and Mg^{2+}, located in the channels within the zeolite framework. The exchangeable cations are only loosely held in the channels and are readily replaced by cations from the surrounding environment [10]. Thus, one of the most interesting applications of zeolites within the food industry is related to their antimicrobial activity against several pathogenic bacteria. In fact, most antimicrobial zeolites are formed by their combination with different oxides or metal ions [11–14]. Silver is one of the most common ions to combine in zeolite frameworks for attaining biological activity by virtue of its high stability and broad spectrum against different types of bacteria, viruses, germs, and fungi [15–17]. Several recent review articles highlighted the mechanisms of antimicrobial activity of silver ions Ag^+ and silver nanoparticles AgNP [15, 18]. In fact, Ag-based nanoparticles have many points of attack within the bacteria cell as well as cell membrane surface, and this multi-pronged effect of Ag^+ is responsible for antimicrobial activity. AgNP promote oxidative stress and DNA damage, inhibit the transport functions in the cell wall (respiration) and the cell division (reproduction) and interrupt the cell energy generation (metabolism).

Many antibacterial packaging films from polymer matrixes and zeolite-loaded silver nanoparticles have been successfully synthesized. Poly(butylene succinate) (PBS) composite films containing three different antibacterial agents; silver zeolite A (AgZ A), silver zeolite Y (AgZ Y), and silver zeolite ZSM-5 (AgZ SM-5), were prepared by solvent casting and melt extrusion methods [16]. The addition of silver zeolite enhanced the antibacterial activity but decreased the mechanical and biodegradable properties of PBS composite films. Carboxy methyl cellulose/poly(vinyl alcohol) (CMC/PVA) films-based zeolite doped with silver cations have shown improved mechanical, water vapor transmission, gas transmission and antimicrobial properties [11]. Furthermore, Diblan et al. [19] assumed that the lowest growth rate regarding total mesophilic aerobic bacteria in count was found in silver-zeolite/low density polyethylene–polyamide nanocomposites, enhancing shelf life of kashar cheese. Silver and Zinc containing zeolite coating was deposited on Bi-axial Oriented Poly Propylene (BOPP) film and its effect of microbial activity was evaluated for bacteria stains which majorly reduces the quality of the meat [20]. It was found that after 4 h exposure in agar test, microbial activity had been reduced up to 92.67% and after 24 h of exposure, the microbial activity further reduced up to 98.5%. The potential application of antibacterial zeolite loaded silver nanoparticles/polymer films in food preservation and safety have also been highlighted for polyethylene [21], polyvinylchloride [22], polyvinyl alcohol [23], chitosane [24], polylactic acid [25], and alginate [26].

Our previous investigations consisting in preparing poly(ε-caprolactone) PCL/montmorillonite [27, 28] and PCL/kaolinite [29] nanocomposite films with supported silver nanoparticles showed good bactericidal properties. Notice that PCL is a thermoplastic biopolymer synthesized from crude oil. PCL is hydrophobic and degrades in bioactive environments. This polymer is highly researched in food packaging domain owing to its long-term stability and controlled release properties [7].

Hence, the present study has been performed to prepare poly (ε-caprolactone)-based nanocomposite films with zeolite-supported silver nanoparticles. Structural, surface properties, thermal, mechanical and water vapor barrier behaviors of these nanocomposites have been investigated, and their antibacterial activity was assessed against both gram-positive and gram-negative bacteria stains.

EXPERIMENTAL

Material

Poly(ε-caprolactone) (reference CAPAR650), with a weight-average molecular weight (M_W) of 49.000 and of polydispersity index of 1.4, was supplied by Solvay Chemicals sector-SBU (Brussels, Belgium). Commercial grade zeolite (reference 4A) belonging to the family of alkaline aluminosilicates was obtained from PQ Chemical Limited (Thailand) and provided by Universal Oil Product (UOP, Des Plaines, Illinois, USA). This crystalline and porous powder had a Si : Al ratio of 1 : 4 and a pore size of between 3.8 and 4 Å. The chemical formula of a fully hydrated pseudo-mesh (corresponding to one eighth of the elemental mesh) of zeolite 4A is ($Na_{12}[(SiO_2)_{12}(AlO_2)_{12}] \cdot 27H_2O$). The silver nitrate ($AgNO_3$) and sodium borohydride ($NaBH_4$) reagents were supplied by Sigma Aldrich (St Louis, Missouri, USA). Aqueous solutions were prepared with double distilled water. All chemicals were used without any further purification.

Preparation of Zeolite-Ag Nanoparticles

Zeolite-silver nanoparticles (AgZ NPs) were prepared according to the procedure described elsewhere [28, 30–32] with slight modifications. A weighed amount of commercial zeolite 4A (10 g) was dispersed in 100 mL of silver nitrate aqueous solution $AgNO_3$ (0.47 mol/L). The mixture was stirred for 24 h in the dark at room temperature using a magnetic stirrer. A freshly prepared $NaBH_4$ aqueous solution (4×10^{-2} M) was then added dropwise to the suspension under continuous stirring until a constant $AgNO_3$: $NaBH_4$ molar ratio (1 : 4) was reached. The obtained suspension was then centrifuged at 4200 rpm for 30 min, and the precipitate was washed 4 times using double distilled water to remove the silver ion residue, and then was dried overnight at 70°C in a vacuum oven. The dried solid samples were ground using a mortar and pestle to form a fine powder.

Preparation of PCL/AgZ Nanocomposite Films

AgZ solutions (2, 3, and 5% w/v) were prepared by dissolving appropriate amounts of AgZ nanoparticles in chloroform. PCL solutions (10% w/v) were prepared using the same solvent. The obtained solutions were then mixed together (1 : 1 v/v) and stirred overnight. The three PCL-2% AgZ, PCL-3% AgZ, and PCL-5% AgZ solutions were thereafter cast onto a 9 cm diameter glass Petri-dish and left for the evaporation of chloroform for 24 h in a fume hood. Similar procedure was followed to prepare the pure PCL polymer, which was used as a control. Films generated from the different polymeric solutions by solvent evaporation were dried in a vacuum oven for several days at 40°C. The final thickness of the films obtained is around 0.4 mm.

Structural and Surface Properties

The dispersion of the AgZ nanoparticles in the PCL matrix were examined by infrared spectroscopy, UV-visible spectroscopy and X-ray diffraction.

Infrared Spectroscopy

Infrared spectra of PCL and PCL-AgZ nanocomposite materials were determined on a Fourier transform spectrophotometer Thermo-Scientific Nicolet® IS5-IR (Massachusetts, USA) equipped with an attenuated total reflection (ATR) accessory containing a diamond/ZnSe crystal. FTIR-ATR spectra were obtained in the range of 400–4000 cm^{-1} at room temperature, using 64 scans and 2 cm^{-1} resolution. The base line of the obtained spectra was corrected in Omnic® software (Massachusetts, USA). Before being analyzed, samples were vacuum-oven dried at 45°C for 48 h in order to eliminate moisture and any trace of solvent.

UV-visible Spectroscopy

The UV-Vis absorption spectra of the aqueous solutions containing as-prepared pure PCL and its nanocomposites PCL/AgZ were recorded in the 300–800 nm wavelength range by using JASCO V-630 Spectrophotometer (Lisses, France).

X-ray Diffraction

X-ray diffraction (XRD) was employed to determine the effect of silver ion exchange on the structure of zeolite and to find out the crystalline phases of PCL/AgZ nanocomposites. All of the samples were analyzed with an X-ray diffractometer (Philips PW3710, Eindhoven, Nederland) with a speed of scattering at 0.05 s^{-1} over a range of angles 2θ between 5° and 50°. The operating current and voltage were fixed at 20 mA and 40 kV respectively. Measurements were performed using CuK_α radiation ($\alpha = 1.5418$ Å).

Water Contact Angle

Water contact angle on the surface (wettability) of neat PCL and its nanocomposite films (strips of 1 × 10 cm) was performed at room temperature using the sessile drop method. A 3 μL liquid drop of ultrapure water was placed on the horizontal surface of each polymer film using a microsyringe. An image of each drop was captured immediately after the droplets were placed onto the surface by a digital camera. The contact angle of each drop was calculated according to the "Laplace-Young" method with an image analysis freeware (ImageJ). Reading was taken twice which was on top and bottom of layer of the membranes, and results are expressed as mean ± standard deviation.

Thermogravimetric Analysis

Thermogravimetric analysis (TGA) was performed on a Q 500 TA Instrument (New Castle, DE, USA). Samples weighing around 5 mg were placed in aluminum pans and heated from 40 to 600°C at a heating rate of 10°C/min under a nitrogen atmosphere, with a flow rate of 40 mL/min.

Differential Scanning Calorimetry

Differential scanning calorimetry (DSC) was used to determine the glass transition temperatures T_g and the melting temperatures T_m of the nanocomposite materials. A Mettler Toledo DSC 3, (Ohio, USA) device preliminarily calibrated with a standard reference of indium was used. About 10 mg of samples were weighed and sealed in a standard aluminium pan, then analyzed under nitrogen gas at 50 mL/min. A baseline was constructed using an empty aluminium pan over the same temperature range and scanning rate. The samples were scanned from 25 to 100°C at a heating rate of 10°C/min (first heating), cooled to –80°C at the same scan rate, then heated again to 100°C at 10°C/min (second heating).

Water Vapor Permeability

The water vapor permeations were performed according to the "cups methods," referring to the standard ISO 7783. A cylindrical vessel filled with 10 g of CaCl_2 desiccant powder was used and sealed with the investigated films. The temperature was set to 23 ± 1°C with a relative humidity of 48 ± 2%. The water mass uptake of the desiccant powder was monitored with time. The water vapor transmission rate (*WVTR*) is then calculated from the slope of the mass uptake profile versus time as soon as the steady state is reached. The water vapor permeability (*WVP*) coefficient was then calculated using the following equation:

$$WVP = \frac{WVTR \times e}{\Delta P}, \tag{1}$$

while e is the film thickness and ΔP is the water vapor partial pressure difference. From the experimental conditions (temperature and relative humidity mentioned above), the water vapor partial pressure ΔP is 1400.3 Pa.

Atomic Force Microscopy

The morphology of PCL and PCL-AgZ nanocomposites films was assessed using atomic force microscopy (AFM) operated in tapping mode with a silicon probe cantilever with a spring constant of 20–60 N/m, nominal tip radius of 5–10 nm, and scan rate of 1 Hz using a Bruker's Dimension Icon (Massachusetts, USA) nanoscope.

Mechanical Tests

The tensile modulus, tensile strength and elongation at break were measured in a Tensile Zwick/Roell Z 100 tester (Ulm, Germany), at a strain rate of 200 mm/min. The films were conditioned in a desic-

Table 1. PCL and PCL/AgZ nanocomposites films characteristics

Film membrane	Contact angle, θ	Surface properties	WVP, g/m 24 h Pa	T_g, °C	T_m, °C	Young modulus, MPa	Yield point, MPa	Strength at break, MPa	Elongation at break, %
PCL	74.4 ± 0.3	Hydrophilic	0.35[a]	–65.5[a]	59.1[a]	4.21 ± 0.01	22.09	29.5	376.4
PCL/AgZ 2%	68.4 ± 0.3	Hydrophilic	0.54	–61.8	57.9	4.29 ± 0.01	23.88	29.17	317.4
PCL/AgZ 3%	59.5 ± 0.6	Hydrophilic	0.45	–68.3	57.6	4.46 ± 0.01	23.34	27.9	303.8
PCL/AgZ 5%	67.8 ± 0.4	Hydrophilic	0.39	–69.5	58.1	4.58 ± 0.05	22.34	27.3	296.3

[a] Previous work published in reference [28].

cator under 50% RH, at 25°C, for 48 h before being characterized.

Antimicrobial Activity

The antimicrobial activity of the pure PCL and PCL/AgZ nanocomposites was assessed against *Staphylococcus aureus* CIP 4.83 (Gram-positive strain), and *Salmonella enteric* CIP 80.39 (Gram-negative strain). The evaluation of antimicrobial activity was carried out quantitatively by enumerating the bacteria that survived by plating on optimal medium (ASTM E2180 test method). A similar protocol was used as described in in our previous work [29].

Specimens of 100 mg were introduced in test tubes containing 9 mL of a buffered sodium chloride–peptone solution, pH 7.0. Subsequently, tubes were inoculated with 1 mL of each bacterium. Control experiments with pristine PCL were performed under the same conditions. All samples were incubated in a wrist-action shaker (150 rpm) at 37°C for 24 h. Afterward, 0.1 mL aliquot from each tube was sown in TSA plates and incubated for 24 h at 37°C. Finally, viable cells were counted. The reduction of bacteria β (%) in the specimen was calculated according to the following equation:

$$\beta(\%) = \frac{N_a - N_b}{N_a} \times 100, \quad (2)$$

where N_a and N_b are the average numbers of viable bacteria after cultivation on TSA plates for 24 h for the blank control (PCL) and test specimen (PCL/AgZ), respectively.

RESULTS AND DISCUSSION

PCL neat polymer and its AgZ nanocomposites properties are summarized in Table 1.

Structural and Surface Properties

The FTIR spectrum of AgZ NPs, presented in previous work [33], particularly displayed a band centered at 3404 cm^{-1} attributed to the elongation vibrations of structural hydroxyls from the isolated silanols, as well as to physisorbed water molecules, whose presence is confirmed by the band at 1650 cm^{-1} linked to the deformation vibrations H–O–H, reflecting the hydrophilic character of zeolite. The bands at 1148 and 712 cm^{-1} are due to asymmetrical and symmetrical Al–O vibrations of the internal tetrahedra, respectively. The bands at 1000 and 776 cm^{-1} are associated with the elongation vibrations of the asymmetrical and symmetrical external Si–O–Si or Si–O–Al bonds. An intense band located at 450 cm^{-1} corresponds to the deformation vibrations of Si–O–Si bonds.

ATR-FTIR spectra of pure PCL and its nanocomposites PCL/AgZ at different nanocharge rates are shown in Fig. 1. Two peaks around 2945 and 2865 cm^{-1} can be assigned respectively to the symmetrical and asymmetrical stretching vibrations of $-CH_2$ group. The characteristic vibrations of linear ester carbonyl groups C=O bond can be observed at 1723 cm^{-1}. The peak localized at 1264 cm^{-1} can be related to the deformation of the C–O–C bond. Further bands between 700–1600 cm^{-1} can be attributed to the skeletal structure of the polymer chain and its nanocomposites [34–36]. Namely, peaks located at around 1100 cm^{-1} on PCL/AgZ nanocomposites indicate M–O–M (M = Al or Si) asymmetric stretching vibrations.

The comparison between pure PCL and its nanocomposites spectra leads to the following remarks.

A displacement of the band characteristic of C=O group from 1723 to 1720 cm^{-1}, which would be due to the presence of any specific interactions of the hydro-

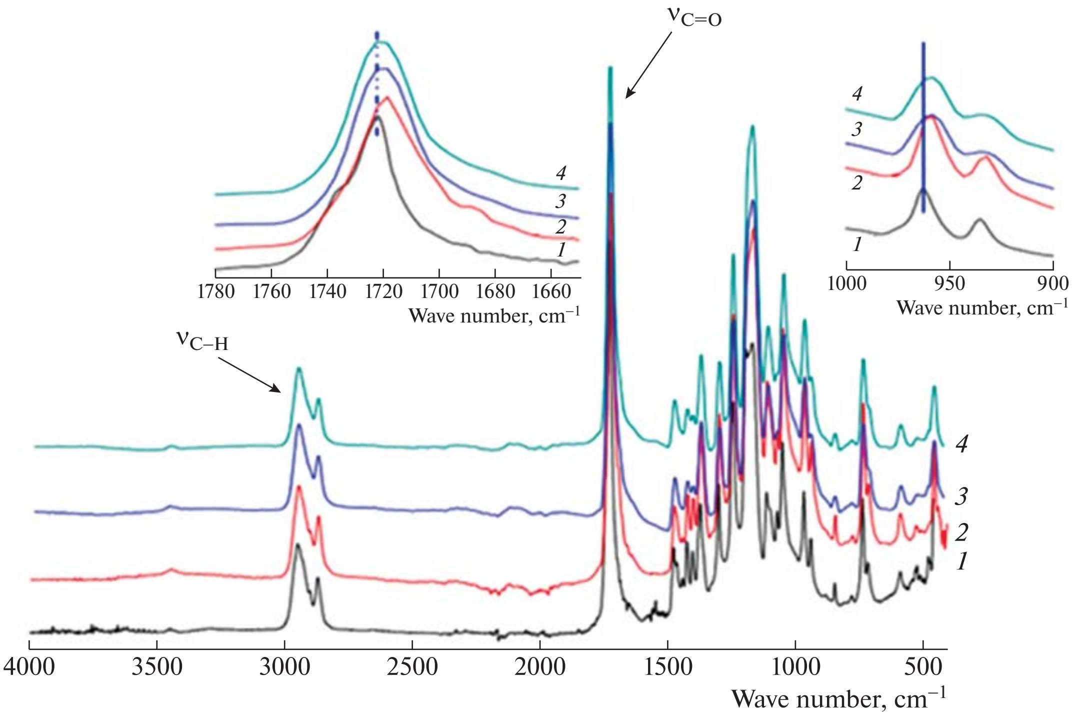

Fig. 1. ATR-FTIR spectra of (*1*) neat PCL and its nanocomposites PCL-AgZ: (*2*) 2, (*3*) 3, and (*4*) 5%.

gen bond type that can be developed between the carbonyl group of the PCL and the nanocharge AgZ. A shift and an increase in the intensity of the shoulder located around 958 cm^{-1} that would be associated with the distribution of the Si–O– groups in their matrix.

The UV-Vis absorption spectra of the aqueous solutions containing as-prepared pure PCL and its nanocomposites PCL/AgZ are shown in Fig. 2. Neat PCL did not show any absorption peak, whereas its PCL/AgZ nanocomposites exhibited a high intensity peak at λ_{max} = 420 nm confirming the existence of small Ag nanoparticles inside the PCL matrix. These peaks characterizing the surface plasmon resonance of spherical silver nanoparticles in good agreements with Shameli et al. [37] and Rong et al. [38] investigations. The intensity and width of absorption peaks of nanocomposites are greater for a high nanocharge AgZ rate, thus indicating the amount of silver nanoparticles increases with the increase of nanofiller. The symmetrical shape UV absorption peaks obtained for the three nanocomposites suggest that nanoparticle size distribution is quite homogeneous.

The XRD patterns of AgZ nanoparticles, PCL and its nanocomposites with various AgZ contents are shown in Figs. 3 and 4, respectively.

Pure zeolite diffractogram showed several diffraction peaks localized at 2θ = 6.16°, 10.12°, 11.91°, 15.65°, 18.68°, 20.46°, 23.66°, 27.05°, 29.7°, 31.44°, 32.45°, 33. 49°, 37.72°, 44.70°, 53.8°, 58.27° reflecting its crystalline structure and absence of amorphous phase [33].

The X-ray diffractogram of silver modified zeolite (Fig. 3), displays four peaks at 2θ = 19.8°, 24.8°, 26.59°, and 34.92° corresponding respectively to the crystallographic planes (220), (311), (320), and (332). It should be noted that the peaks corresponding to Ag compounds were observed after cation exchange procedure around 2θ = 38.08°, 44.18°, 61.13°, 77.24° corresponding respectively to (111), (200), (220), and (311) crystallographic planes of the face-centered cubic silver crystals indicating that this metal is highly dispersed in the zeolite hosts (standard diffraction pattern of ref. 01-087-0717) [37, 39]. The crystallinity was obtained by comparing the intensities of the four peaks assigned to (111), (200), (440), (220), and (311) reflections, based in ASTM D 3906-80 method. For all samples, the XRD patterns of Ag-zeolites presents over 95% of crystallinity [40].

Benhacine et al. [28] reported that PCL XRD pattern is characterized by two peaks approximately at 2θ = 21° and 24° corresponding to the (110) and (200) crystallographic planes, respectively, revealing the crystalline structure of PCL (Fig. 4). It can be shown that the crystalline structure of PCL nanocomposite materials does not change after adding AgZ nanoparticles. Nevertheless, an increase of the intensity of these two characteristic peaks is noted reflecting an increase in crystallinity of the PCL matrix [41]. This increase is attributed to the incorporation of effective

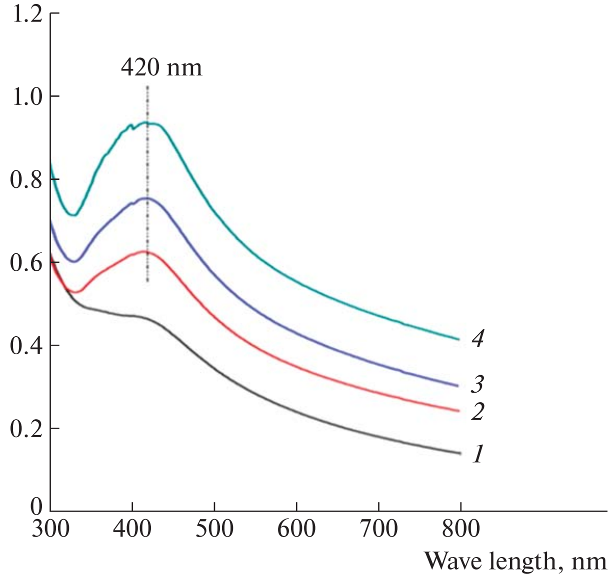

Fig. 2. UV-visible spectra of (*1*) PCL and its nanocomposites PCL/AgZ: (*2*) 2, (3) 3, and (*4*) 5%.

nucleation agent AgZ and its satisfactory dispersion in the PCL matrix.

Taking the wetting of a water droplet on a flat surface, if the contact angle is less than 90°, the surface exhibits hydrophilic properties; if the contact angle is more than 90°, the surface exhibits hydrophobic properties [42]. As it can be seen on Table 1 and Fig. 5, the water contact angle of neat PCL was 71° while its AgZ nanocomposites had contact angles ranging between 54.3° and 60.7°, exhibiting hydrophilic properties. This implies that, in an ambient environment with a relatively high RH, the adhesive force between PCL based films and the other hydrophilic surface could be mainly capillary force [43].

Sultana et al. [36] demonstrated that PCL and PCL-zeolite membranes have a hydrophobic behavior with water contact angles of 107.7° and 119.5°, respectively, indicating a lower wetting tendency. However, the introduction of silver nanoparticles (AgNPs) into PCL matrixes induces a decrease in the contact angle [44–46]. Thus, as obvious from Table 1, the contact angle exhibited a decreasing trend from 71.0° to 54.3° for neat PCL and PCL/AgZ 5%, respectively, leading to more hydrophilic materials in good agreement with the literature. This increase in hydrophilicity could be attributed to a decreased in surface roughness at higher Ag contents [44]. The increase in hydrophilicity is a desirable characteristic in antimicrobial polymer materials as it has been commonly observed that pathogenic bacteria adhere more on hydrophobic polymers [47].

Thermal Properties

The thermal stability study of zeolite before and after AgNPs formation was carried out under nitrogen flow up to 700°C and continuedunder nitrogen/oxygen flow up to 1000°C to verify the presence ofAgNPs in AgZ and the results [33]. Under inert atmosphere, AgZ showed a single weight loss step of 10% at around 104.76°C. The latter was attributable to moisture loss, which was greater for the unloaded zeolite than for the one loaded with AgNPs due to its hydrophilic character. Meanwhile, after the application of a mixed nitrogen/oxygen atmosphere, the AgZ thermogram showed immediate oxidative decomposition at $T_{\max}$ of 710°C, indicating the formation of metal oxides upon

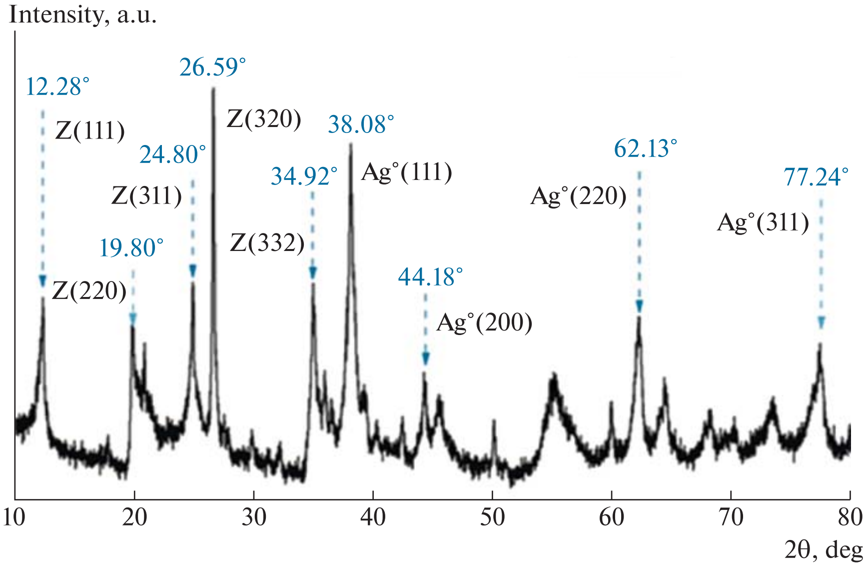

Fig. 3. XRD pattern of AgZ nanoparticles.

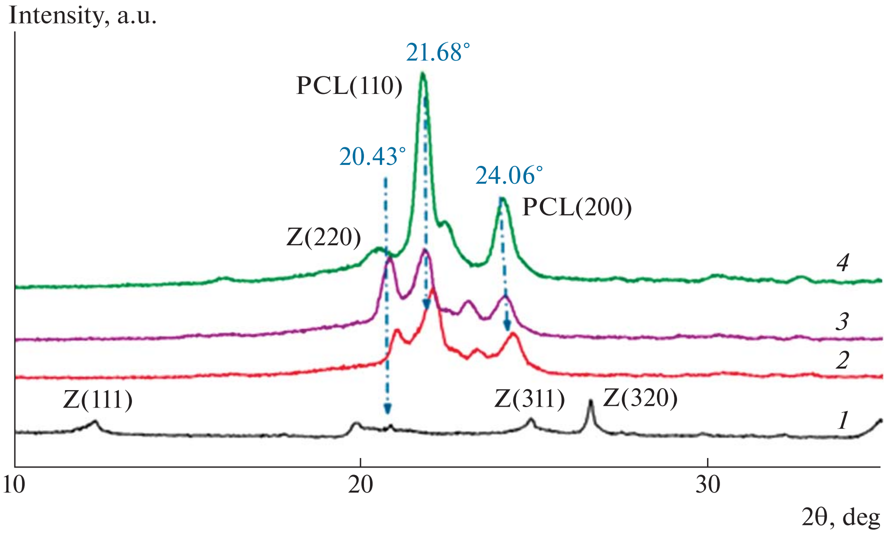

Fig. 4. XRD patterns of (*1*) PCL and PCL zeolite-silver containing nanocomposites: (*2*) 2, (*3*) 3, and (*4*) 5%.

interaction with oxygen atoms, which are subsequently eliminated.

Thermogravimetric analysis is one of the most common techniques for analyzing the thermal properties of polymer materials used in food packaging and evaluating their thermal stability during the application (namely in freezing and heat treatment of food).

Figure 6 illustrates the TGA curves and respective first derivative curves in nitrogen atmosphere for neat PCL and its nanocomposites with different loadings of AgZ. As can be seen, all the samples exhibit remarkably good thermal stability since no mass loss occurred until 300°C. It can be observed that the thermal degradation of PCL occurs in one-step, attributed to the PCL decomposition into methyl pentanoate, water and carbon dioxide [48]. Whereas, it has been reported in the literature that the thermal degradation of PCL occurs in two stages [49]. The first process implies a statistical rupture of the polyester chains via ester pyrolysis reaction. The produced gases were identified as H_2O, CO_2, and 5-hexenoic acid. The second step leads to the formation of ε-caprolactone (cyclic monomer) as result of an unzipping depolymerization process.

It is quite visible that the degradation of the nanocomposites materials occurs at lower temperatures than in pure PCL, and the thermal degradation temperature T_{onset} decreases gradually when the charge amount of AgZ is increased (Fig. 6a). It can be assumed that high concentrations of zeolite nanoparticles accelerate the formation of polymer radicals leading to a reduction in the thermal stability of the material. Consequently, temperatures at which maximum weight loss occurs $T_{\max}$ decreases when AgZ quantity increases in PCL matrix (Fig. 6b). It can be concluded that AgZ nanoparticles have a catalytic effect on the thermal decomposition of PCL matrix due to the presence of Lewis acidic sites created upon organic modifier degradation.

The residue for neat PCL is about 0.4% at 500°C, whereas in the other samples it ranged between 2 and 10% due to the presence of AgZ nanocharge.

The DSC thermal curves obtained for PCL/AgZ nanocomposite films are presented in Fig. 7. The obtained thermograms showed that the samples did not undergo degradation during the heating process. To remove any traces of volatile compounds incrusted in the polymer materials, such as solvent, water, and residual monomer, the glass transition temperature T_g,

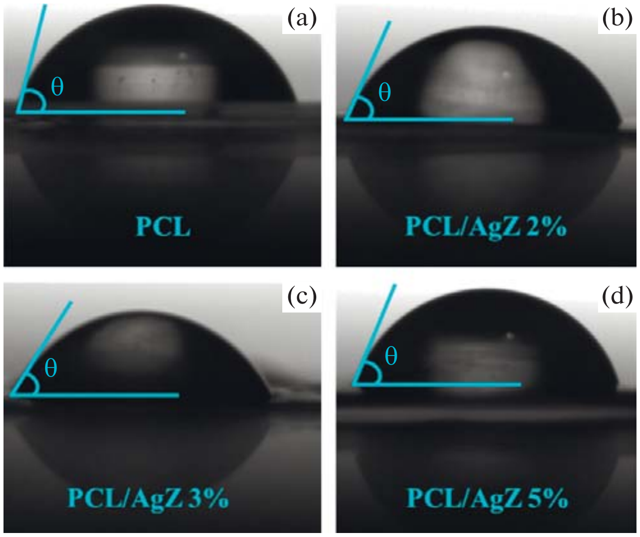

Fig. 5. Optical photograph of a drop of water on (a) neat PCL and PCL/AgZ nanocomposites films: (b) 2, (c) 3, and (d) 5%.

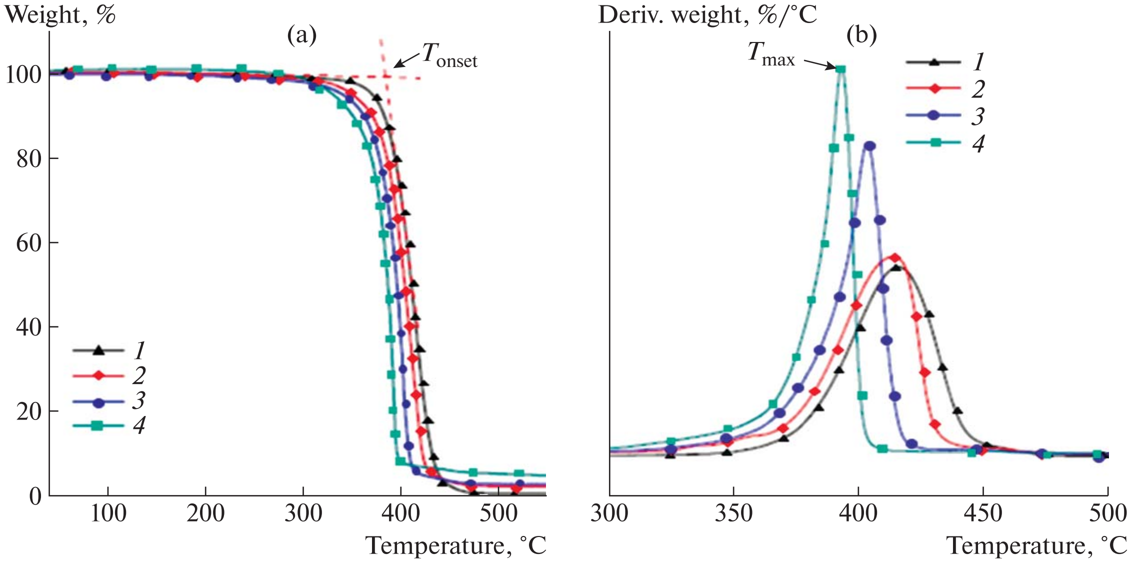

Fig. 6. (a) Thermogravimetriccurves and (b) differential thermogravimetric curves of (*1*) pure PCL and its nanocomposites PCL/AgZ: (*2*) 2, (*3*) 3, and (*4*) 5%.

and the melting temperature T_m of the samples were taken from the second cycle of the DSC process. These parameters were accurately determined on the thermograms from the midpoint indicating the variation in the heat capacity versus temperature and are summarized in Table 1.

Besides the glass transition temperature (T_g below −65.5°C), PCL/AgZ nanocomposite present an endothermic peak around 58°C, which is ascribed to the melting temperature T_m owing to its semi-crystalline structure. T_g and T_m values are not significantly affected by AgZ loading. In a previous investigation, it was evidenced that the melt crystallization temperature T_c increased with the nanofiller loading. This increase is attributed to the incorporation of effective nucleation agent AgZ and its satisfactory dispersion in the PCL matrix [28].

Water Vapor Permeability

In food packaging materials, the water vapor permeability (WVP) is of significant importance with regard to the control of moisture transferred between the food and the exterior environment. A high WVP can lead to the microbial spoilage of food. The absolute value of water vapor permeability through nanocomposites films is governed by the polymer type, the filler type, the concentration and the aspect ratio.

The WVP values measured for PCL/AgZ nanocomposite films calculated according to Eq. (1) are presented in Table 1.

It can be observed that PCL/AgZ nanocomposite films showed a slightly higher WVP compared to pure PCL. This can be attributed to the hydrophilic property of zeolite nanoclay since the major constituent of zeolite clays is silica, and silica particles are impermeable to water vapor [7]. However, all nanocomposites had acceptable water vapor permeability values, which decreased from 0.54 g/m 24 h Pa for PCL/AgZ 2% to 0.39 g/m 24 h Pa for PCL/AgZ 5% reflecting an improved water barrier properties with nanofiller concentration. The decrease in water vapor permeability with increasing mass content of the filler may be due to physical adsorption characteristics of zeolites.

Atomic Force Microscopy

AFM was applied to provide information about the nanostructure of nanocomposite films. Figures 8 and 9 depict the 3D-topographical views of neat PCL and PCL/AgZ nanocomposites respectively. The dark regions represents valleys or membrane pores and brightest regions represents highest points or nodules of the membrane surface. Table 2 summarizes 3D-surface roughness parameter values of PCL/AgZ nanocomposites.

Neat PCL surface membrane shows a smooth topography with some minor surface irregularities (see Fig. 8). The introduction of AgZ nanoparticles into PCL matrix leads to significant changes in membranes morphology (Fig. 9). The nanocomposite film surfaces changed into fibrillary morphology with an increase in peak and valley counts with increasing AgZ nanoparticles, from 4 and 8 to 33 and 45 for PCL/AgZ 2% and PCL/AgZ 3%, respectively (see Table 2). This increase may be attributed to the creation of cavities inside PCL matrix in which the AgZ nanoparticles have been inserted leading to exfoliated nanocompos-

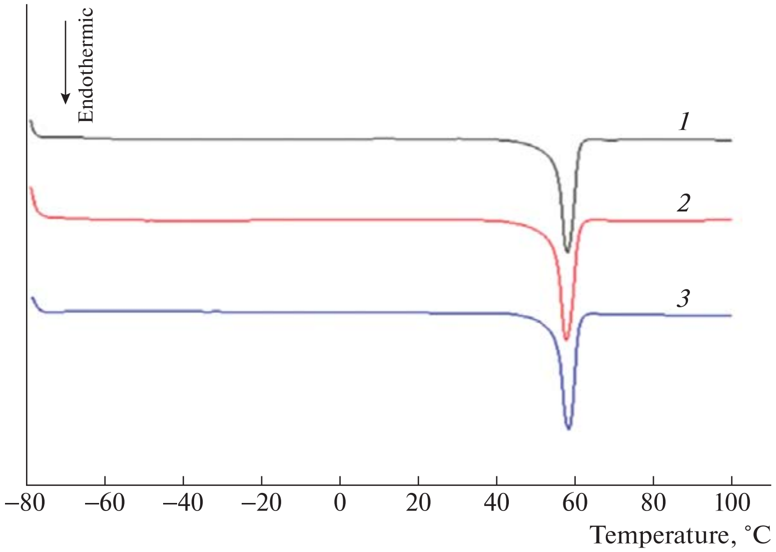

Fig. 7. DSC thermographs of PCL/AgZ nanocomposites: (*1*) 2, (*2*) 3, and (*3*) 5%.

ite materials. Similar structural observations have been noticed for PCL/ bentonite and PCL/ montmorillonite nanocomposites [50–52].

Moreover, the obtained roughness parameter values R_a, R_q, R_{max}, and R_m (displayed on Table 2) decreased for PCl/AgZ 3% nanomaterial. This shows that on addition of AgZ nanoparticles, the nanocomposite membranes have become smoother. The skewness values S_K for both membranes were relatively low (0.09 and –0.12 for PCl/AgZ 2% and PCl/AgZ 3%, respectively) indicating a symmetrical morphology with a good dispersion of AgZ nanoparticles in film membranes, while the kurtosis values ($K_u > 3$) indicate a flattened surfaces.

Mechanical Tests

Tensile properties of PCL and PCL/AgZ nanocomposites were studied and data are summarized in Table 1.

The stress-strain diagram is presented in Fig. 10. It can be seen that PCL and its nanocomposites have a ductile plastic material behavior. The incorporation of AgZ nanoparticles into PCL matrix led to a slight increase of the elastic modulus (from 4.21 MPa for pure PCL to 4.58 MPa for PCL/AgZ 5%). The yield point indicating the elastic limit of these polymer materials increased when AgZ nanoparticles were incorporated into PCL matrix (from 22.09 MPa for pure PCL to 23.38 MPa for PCL/AgZ 2%). This elastic behavior is due to the increase of restoring forces between polymer chains with nanofiller concentration.

Moreover, it can be observed that the addition of AgZ nanoparticles into PCL matrix results in reduced values of the strength at break and the elongation at break (from 29.5 to 27.3 MPa and from 376 to 296% for pure PCL and PCL/AgZ 5%, respectively).

In fact, nanocomposites strength depends on the filler/matrix bonding under large strain conditions [53]. In a nanocomposite, stress is generally transferred from the matrix to the filler through interfacial shear, and interfacial bonds are modified when strain exceeds a critical value [54]. Based on that, our findings may be attributed to the rearrangement of the nanocomposites microstructures under large strain values which is probably due to modification of nanofiller-matrix bonding, leading to an increase in randomly intercalated and/or exfoliated structures of PCL/AgZ nanocomposites for high nanofiller concentrations.

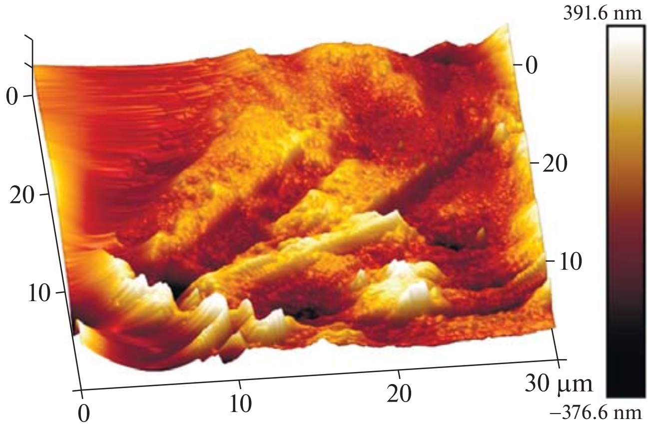

Fig. 8. 3D AFM images of neat PCL membrane.

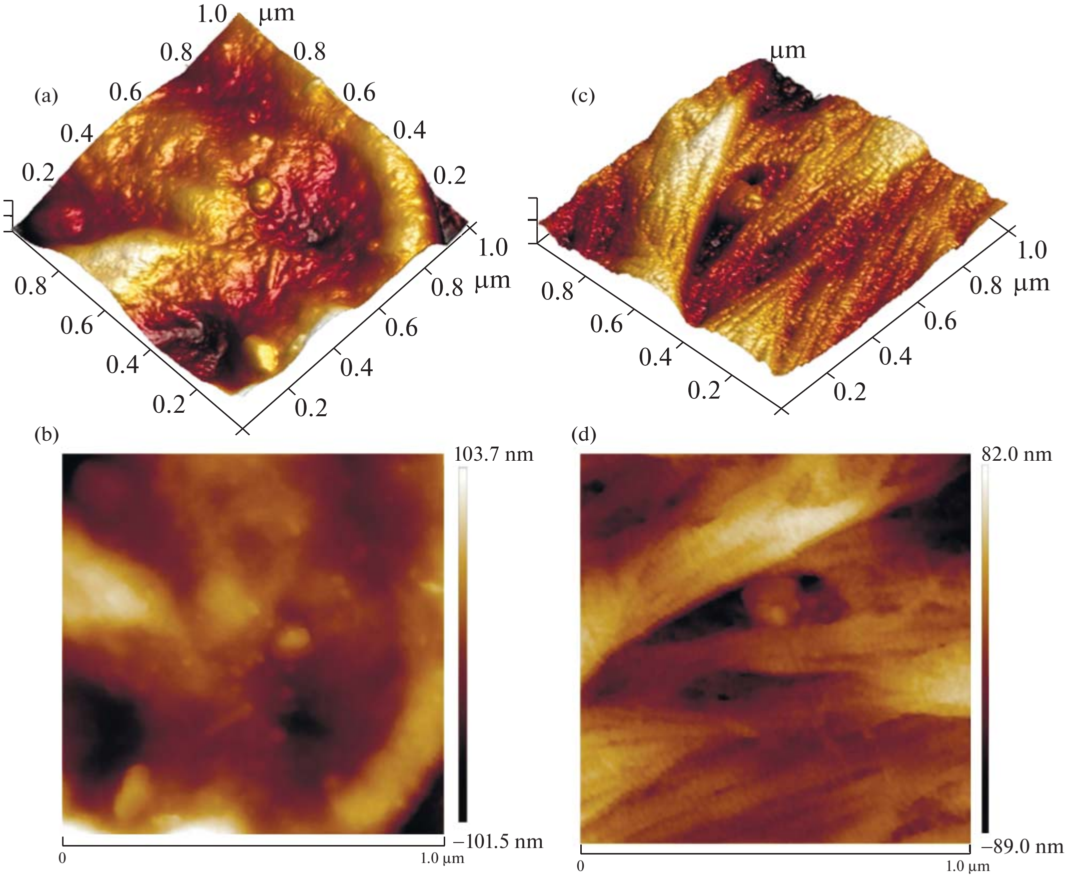

Fig. 9. (a, c) AFM 3D and (b, d) 2D topographic images of PCl/AgZ nanocomposites: (a, b) PCL/AgZ 2%, (c, d) PCL/AgZ 3%.

Antimicrobial Activity

Silver nanoparticles dispersed on zeolite were evaluated as biocides for *Escherichia coli* and *Salmonellatyphi* by Guerra et al. [55]. In this work, AgZ NPs were shown to be efficient in eliminating both these bacteria strains present in nutritive media at times as short as 60 min. Moreover, silver did not leach from the zeolite during the experiments with both *Escherichia coli* and *Salmonella*; thus, it was concluded that the obtained biocidal materials can be reused.

The antimicrobial activity of PCL and PCL/AgZ nanocomposites against *Staphylococcus aureus* and *Salmonella* was measured using the viable cell counting method. The obtained results are presented in Fig. 11 and Table 3.

As shown in Table 3, pure PCL does not show any antimicrobial activity. The number of each strain of bacteria in PCL sample compared to the inoculum remains almost constant. However, after the addition of AgZ nanoparticles into PCL matrix, a significant decrease in the number of bacteria cells is noticed. This is mainly due to the diffusion of Ag^+ ions, associated with pores of zeolite to the culture medium. Once released, the latter could interact with the bacterial strains according to three major pathways: degradation of cell membrane and cell wall, entry into the cell and metabolism disruption, or oxidative stress [56].

Table 2. 3D-surface roughness parameter values of PCL/AgZ nanocomposites

	Peak count	Valley count	R_a, nm	R_q, nm	R_m, nm	R_v, nm	R_{vm}, nm	S_k	K_u
PCL/AgZ 2%	4	8	23	29.4	51.2	−52.8	−29.9	0.09	3.27
PCL/AgZ 3%	33	45	18.5	24	6.58	−86.8	−7.42	−0.12	3.18

R_a: Roughness average, R_q: root mean square roughness, R_m: average height of the analysed area, R_v: maximum profile valley depth, R_{vm}: average max depth, S_k: skewness, K_u: kurtosis.

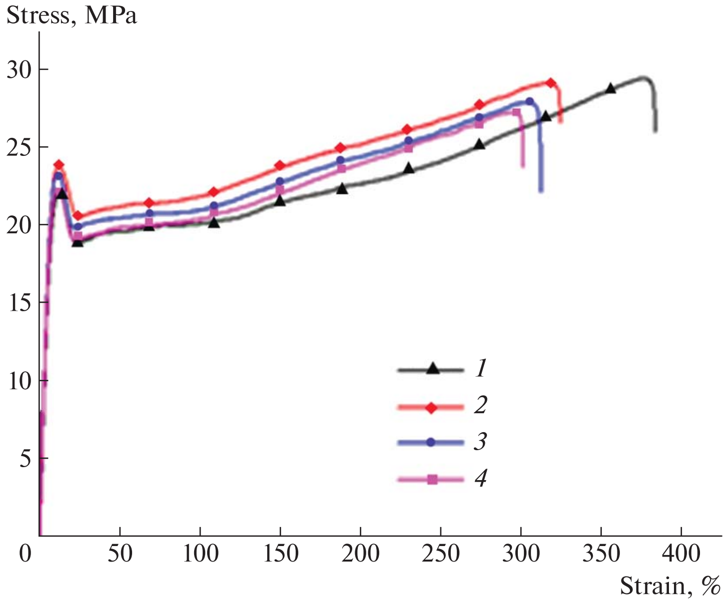

Fig. 10. Tensile properties on (*1*) pure PCL and its AgZ nanocomposites: (*2*) 2, (*3*) 3, and (*4*) 5%.

	PCL/AgZ 2%	PCL/AgZ 3%	PCL/AgZ 5%
S. aureus	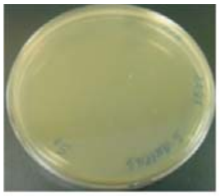	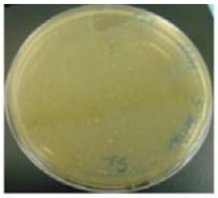	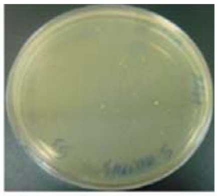
Salmonella	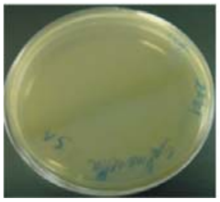	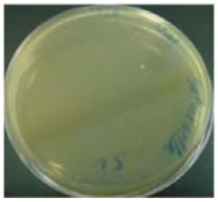	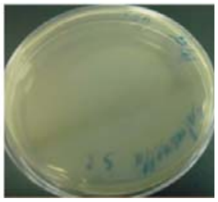

Fig. 11. Growth of the different bacteria in the presence of PCL/AgZ nanocomposites.

It can be also noticed that the antimicrobial activity of both samples is better against *Salmonella* (with a reduction of bacteria up than 91%) than *S. aureus*. In accordance with this, several researchers found that the gram-negative bacterial strains were more susceptible to AgNPs than the Gram- positive bacterial strains [37, 39, 44, 57]. For instance, the minimal inhibitory concentration (MIC) of AgZ nanoparticles was 3.125 μg/mL against *E. coli* gram-negative strain, and 6.25 μg/mL against *Listeria monocytogenes* gram-positive strain [23]. This unlike response towards the gram-negative and gram-positive bacteria could be ascribed to the difference in cell wall structure of those microorganisms. It is assumed that gram-positive bacteria are composed of three-dimensional thick peptidoglycan (~20–80 nm) of linear polysaccharide chains, forming a complex structure through cross-linking with shorter peptides and make AgNPs more difficult to penetrate into intracellular space [26]. In comparison, the gram-negative bacteria strains possess a negatively charged outer membrane and a thin peptidoglycan layer (~7–8 nm), which facilitate the anchoring and penetrating of the silver nanoparticles [57]. However, many other antimicrobial tests revealed that AgNPs are easier to enter into the gram-positive bacteria than gram-negative ones [58, 59],

Table 3. Growth of *S. aureus* and *Salmonella* in the presence of neat PCL and PCL/AgZ nanocomposites

	Inoculum	PCL	PCL/AgZ 2%		PCL/AgZ 3%		PCL/AgZ 5%	
	N_0*	N_a*	N_b*	β, %	N_b*	β, %	N_b*	β, %
S. aureus	638	630	112	82.22	483	23.65	494	21.59
Salmonella	499	533	9	98.31	44	91.74	15	97,19

* Expressed as CFU × 10^6.

suggesting that the antimicrobial activity of the AgNPs is not truly based on the cell wall structure of the bacterial strains. Some other explanations on the antimicrobial action of AgNPs have also been proposed. When the AgNPs enter a bacterial cell, they bind to the proteins and cause conformational changes thus converting them into other less stable states affecting their functions [60]. Moreover, AgNPs interact with and disrupt DNA-phosphorus containing macromolecules, thereby generating reactive oxygen species that disrupt replication pathways resulting in cell death [61, 62]. Furthermore, the AgNPs are believed to inactivate the bacterial enzymes containing thiol groups by generating a high proton motive force strength, resulting in cell growth inhibition [60].

The reduction of bacteria β (%) calculated according to Eq. (2), was found to be greater for PCL/AgZ 2% (82.22% for *S. aureus*, and 98.31% for *Salmonella*), suggesting that a good antimicrobial activity of PCL/AgZ nanocomposites can be achieved by using low concentrations of AgZ nanoparticles.

CONCLUSIONS

In this study, PCL/AgZ nanocomposite membranes were successfully fabricated by solvent casting method using chloroform solvent. Through experimental measurements of their physicochemical properties, it was found that the nanocomposite membranes elaborated exhibit good surface homogeneity with hydrophilic properties. An increase in crystallinity of the PCL matrix was noticed when AgZ nanoparticles were added, indicating that latter had an effective nucleation effect. PCL polymer and its AgZ nanocomposites were thermally stable until 300°C and decomposed according to a one-step decomposition process. However, AgZ nanoparticles led to a decrease in thermal stability of PCL polymer matrixes due to their catalytic effect on their thermal decomposition. In addition, PCL/AgZ based films exhibited bactericidal performance against *S. aureus* and *Salmonella* as demonstrated by a clear inhibition of the bacterial growth.

In accordance with the obtained results, it is evident that the developed nanocomposite material based on PCL/AgZ nanoparticles broaden the practical applications of these polymer materials to fabricate biodegradable plastics as an active food packaging.

FUNDING

This work was supported by ongoing institutional funding. No additional grants to carry out or direct this particular research were obtained.

CONFLICT OF INTEREST

The authors of this work declare that they have no conflicts of interest.

REFERENCES

1. V. M. Rangaraj, K. Rambabu, F. Banat, and V. Mittal, Food Biosci. **43**, 101251 (2021).
2. S. M. El-sayed and A. M. Youssef, Sustainable Food Technol. **1**, 215 (2023).
3. M. V. Nikolic, Z. Z. Vasiljevic, S. Auger, and J. Vidic, Trends Food Sci. Technol. **116**, 655 (2021).
4. A. Jayakumar, S. Radoor, J. T. Kim, J. W. Rhim, J. Parameswaranpillai, D. Nandi, R. Srisuk, and S. Siengchin, Food Packag. Shelf Life **34**, 100967 (2022).
5. M. Z. Akram, S. Yaman Fırıncıoğlu, H. Jalal, and S. Canoğulları Doğan, Turk. J. Agric. Food Sci. Technol. **7**, 1799 (2019).
6. C. C. Villa, G. A. Valencia, A. López Córdoba, R. Ortega-Toro, S. Ahmed, and T. J. Gutiérrez, Food Biosci. **46**, 101577 (2022).
7. X. A. Films and D. S. Naidu, Polymers **12**, 2279 (2020).
8. S. Demirci, Z. Ustaolu, G. A. Yilmazer, F. Sahin, and N. Baç, Appl. Biochem. Biotechnol. **172**, 1652 (2014).
9. A. Gandhi and M. M. Faruque Hasan, Comput. Chem. Eng. **155**, 107548 (2021).
10. M. Osacký, T. Binčík, B. Hudcová, M. Vítková, H. Pálková, P. Hudec, P. Bačík, and A. Czímerová, Heliyon **8**, 12029 (2022).
11. H. F. Youssef, M. E. El-Naggar, F. K. Fouda, and A. M. Youssef, Food Packag. Shelf Life **22**, 100378 (2019).
12. L. Wang, D. D. Dionysiou, W. Wu, H. Chen, X. Xie, and J. Lin, Chemosphere **229**, 1 (2019).
13. A. A. Alswat, M. Bin Ahmad, T. A. Saleh, M. Z. Bin Hussein, and N. A. Ibrahim, Mater. Sci. Eng., C **68**, 505 (2016).

14. E. Alrin, C. R. Tjampakasari, and Y. K. Krisnandi, Inorg. Chem. Commun. **144**, 109943 (2022).
15. P. Dutta and B. Wang, Coord. Chem. Rev. **383**, 1 (2019).
16. N. Wattanawong and D. Aht-Ong, Polym. Degrad. Stab. **183**, 109459 (2021).
17. M. P. Moisés, C. T. Cleiser, C. A. A. Silva, J. G. Meneguin, G. G. Fonseca, M. R. Guilherme, A. W. Rinaldi, E. M. Girotto, and E. Radovanovic, Mater. Lett. **308**, 131194 (2022).
18. S. A. Ahmad, S. S. Das, A. Khatoon, M. T. Ansari, M. Afzal, S. Hasnain, and A. K. Nayak, Mater. Sci. Energy Technol. **3**, 756 (2020).
19. Z. Jelonek, A. Drobniak, M. Mastalerz, and I. Jelonek, Int. Diary J. **140**, 105596 (2023).
20. R. Prabhu and A. Devaraju, Mater. Today Proc. **5**, 14553 (2018).
21. D. L. Boschetto, L. Lerin, R. Cansian, S. B. C. Pergher, and M. Di Luccio, Chem. Eng. J. **204–205**, 210 (2012).
22. D. Zampino, T. Ferreri, C. Puglisi, M. Mancuso, R. Zaccone, R. Scaffaro, and D. Bennardo, J. Mater. Sci. **46**, 6734 (2011).
23. M. J. Kim, T. H. Oh, S. S. Han, S. W. Joo, H. Y. Jeon, and D. W. Chang, Fibers Polym. **15**, 101 (2014).
24. K. L. M. Taaca and M. R. Vasquez, Appl. Surf. Sci. **432**, 324 (2018).
25. A. Fernández, E. Soriano, P. Hernández-Muñoz, and R. Gavara, J. Food Sci. **75**, 186 (2010).
26. S. Shankar, L. F. Wang, and J. W. Rhim, Carbohydr. Polym. **146**, 208 (2016).
27. F. Yahiaoui, F. Benhacine, H. Ferfera-Harrar, A. Habi, A. S. Hadj-Hamou, and Y. Grohens, Polym. Bull. **72**, 235 (2015).
28. F. Benhacine, A. S. Hadj-Hamou, and A. Habi, Polym. Bull. **73**, 1207 (2016).
29. F. Benhacine, A. Ouargli, and A. S. Hadj-hamou, Polym. Plast. Technol. Eng. **58**, 1 (2018).
30. S. Beisl, S. Monteiro, R. Santos, A. S. Figueiredo, M. G. Sánchez-Loredo, M. A. Lemos, F. Lemos, M. Minhalma, and M. N. de Pinho, Water Res. **149**, 225 (2019).
31. D. V. Quang, P. B. Sarawade, A. Hilonga, J. K. Kim, Y. H. Shim, G. N. Shao, and H. T. Kim, Mater. Lett. **68**, 350 (2012).
32. N. N. Volkova, L. M. Bogdanova, L. I. Kuzub, and N. N. Dremova, Polym. Sci. Ser., B **57**, 31 (2015).
33. T. Benhalima, A. Sadi, N. Dairi, and H. Ferfera-Harrar, Sep. Purif. Technol. **342**, 127001 (2024).
34. A. Abdolmaleki and Z. Mohamadi, Colloid Polym. Sci. **291**, 1999 (2013).
35. K. Phillipson, J. N. Hay, and M. J. Jenkins, Thermochim. Acta **595**, 74 (2014).
36. N. Sultana, M. S. I. Rusli, and M. I. Hassan, J. Appl. Membr. Sci. Technol. **21**, 25 (2017).
37. K. Shameli, M. B. Ahmad, Z. Mohsen, W. Z. Yunus, and N. A. Ibrahim, Int. J. Nanomed. **6**, 331 (2011).
38. R. He, X. Qian, J. Yin, and Z. Zhu, Mater. Chem. **12**, 3783 (2002).
39. M. M. Salim, N. Ahmad, and N. Nik, Mater. Sci. Eng. C **59**, 70 (2016).
40. L. Ferreira, A. M. Fonseca, G. Botelho, C. Almeida-Aguiar, and I. C. Neves, Microporous Mesoporous Mater. **160**, 126 (2012).
41. H. Zhang, F. Zhang, L. Yang, Y. Jiang, and Q. Yu, Polym. Sci., Ser. B **58**, 479 (2016).
42. L. Kock-Yee, J. Phys. Chem. Lett. **5**, 686 (2014).
43. R. Jones, H. M. Pollock, J. A. S. Cleaver, and C. S. Hodgest, Langmuir **18**, 8045 (2002).
44. M. K. Ahmed, M. A. Zayed, S. I. El-dek, M. A. Hady, D. H. El Sherbiny, and V. Uskoković, Bioact. Mater. **6**, 2070 (2021).
45. A. Scaffolds, A. Wibowo, G. U. N. Tajalla, M. A. Marsudi, G. Cooper, L. A. T. W. Asri, F. Liu, H. Ardy, and P. J. D. S. Bartolo, Molecules **26**, 1 (2021).
46. F. Bayram, F. Sevgi, and S. Dursun, Colloids Surf., A **653**, 129969 (2022).
47. P. A. Tran, D. M. Hocking, and A. J. O. Connor, Mater. Sci. Eng., C **47**, 63 (2015).
48. K. del Ángel-Sánchez, C. I. Borbolla-Torres, L. M. Palacios-Pineda, N. A. Ulloa-Castillo, and A. Elías-Zúñiga, Polymers **11**, 1955 (2019).
49. O. Persenaire, M. Alexandre, P. Degée, and P. Dubois, Biomacromolecules **2**, 288 (2001).
50. B. Zhu, Y. Wang, H. Liu, J. Ying, C. Liu, and C. Shen, Compos. Sci. Technol. **190**, 108048 (2020).
51. S. Nivedita and S. Joseph, J. Water Process Eng. **21**, 61 (2018).
52. J. Ahmed, R. Auras, T. Kijchavengkul, and S. K. Varshney, J. Food Eng. **111**, 580 (2012).
53. C. L. Wu, M. Q. Zhang, M. Z. Rong, and K. Friedrich, Compos. Sci. Technol. **65**, 635 (2005).
54. E. Sadeghpour, H. Wang, Y. Guo, D. H. C. Chua, and V. P. W. Shim, Composites, Part A **129**, 105729 (2020).
55. R. Guerra, E. Lima, M. Viniegra, A. Guzmán, and V. Lara, Microporous Mesoporous Mater. **147**, 267 (2012).
56. T. C. Dakal, A. Kumar, R. Majumdar, and V. Yadav, Front. Microbiol. **7,** 1831 (2016).
57. R. Yoksan and S. Chirachanchai, Mater. Sci. Eng., C **30**, 891 (2010).
58. B. Gu, Q. Jiang, B. Luo, C. Liu, J. Ren, X. Wang, and X. Wang, Carbohydr. Polym. **260**, 117835 (2021).
59. M. Sprynskyy, H. Sokol, K. Rafińska, W. Brzozowska, V. Railean-Plugaru, P. Pomastowski, and B. Buszewski, Colloids Surf., B **180**, 457 (2019).
60. S. Wahab, T. Khan, M. Adil, and A. Khan, Heliyon **7**, e07448 (2021).
61. I. Laib, B. Djahra Ali, and O. Boudebia, J. Organomet. Chem. **986**, 122619 (2023).
62. A. O. El-Gendy, A. Samir, E. Ahmed, C. S. Enwemeka, and T. Mohamed, J. Photochem. Photobiol., B **223**, 112300 (2021).